

Direct Observation of Worm-Like Nanochannels and Emergent Magnon Motifs in Artificial Ferromagnetic Quasicrystals

Sho Watanabe, Vinayak S. Bhat, Korbinian Baumgaertl, and Dirk Grundler*

Quasicrystalline structures and aperiodic metamaterials find applications ranging from established consumer gadgets to potential high-tech photonic components owing to both complex arrangements of constituents and exotic rotational symmetries. Magnonics is an evolving branch of magnetism research where information is transported via magnetization oscillations (magnons). Their control and manipulation are so far best accomplished in periodic metamaterials which exhibit properties artificially modulated on the nanoscale. They give rise to functional components, such as band stop filters, magnonic transistors and nanograting couplers. Here, spin-wave excitations in artificial ferromagnetic quasicrystals created via aperiodic arrangement of nanoholes are studied experimentally. Their ten-fold rotational symmetry results in multiplexed magnonic nanochannels, suggesting a width down to 50 nm inside a so-called Conway worm. Key elements of design are emergent magnon motifs and the worm-like features which are scale-invariant and not present in the periodic metamaterials. By imaging wavefronts in quasicrystals, insight is gained into how the discovered features materialize as a dense wavelength division multiplexer.

standing their perfect growth and the generation of defects along the so-called Conway worms, that is, characteristic chains of tiles in 2D quasicrystals.^[4,5] The underlying mathematical concepts^[6–8] and state-of-the-art nanofabrication techniques allow researchers nowadays to explore aperiodicity-induced effects based on a materials-by-design approach.^[9] In photonics, artificial quasicrystals composed from nanoholes in thin dielectrics provoked distinct optical responses offering advanced manipulation of light waves.^[10–12] In magnonics,^[13] an evolving branch of magnetism exploring spin waves (SWs, magnons) to transmit and process information, periodically modulated magnetic materials have been explored to modify SWs and contributed to the realization of miniaturized microwave devices offering GHz signal processing.^[14,15] Magnonic crystals tailored the band structure of SWs and allowed one to create band stop

1. Introduction

Quasicrystals^[1] are long-range ordered materials that exhibit aperiodicity and rotational symmetry forbidden in conventional crystals.^[2] Aperiodicity makes the understanding of wave propagation a complex challenge as the Bloch theorem cannot be applied to quasicrystals.^[3] Similar challenges exist for under-

filters.^[13] Via non-linear magnon–magnon scattering in a magnonic crystal, all-magnon based information processing was realized.^[16] Periodically arranged nanostructures on ferromagnetic thin films performed as microwave-to-magnon transducers. They provided reciprocal lattice vectors \mathbf{G} allowing to shorten wavelengths of microwave signals by several orders of magnitude.^[17,18]

There is a great interest in studying static and microwave magnetodynamics in artificial quasicrystal spin ices made of connected or disconnected nanobars on Penrose and Ammann quasicrystal lattices.^[19–21] From a fundamental physics perspective, quasicrystal artificial spin ices help towards answering the long-standing fundamental question of how aperiodicity influences the static and dynamic magnetic properties. From an application perspective, one of the main foci of the study of aperiodic quasicrystal spin ices is towards fabricating magnonic crystals with complete band gaps and omnidirectional grating couplers, enabled by the manifold rotational symmetries which go beyond the so far exploited periodic Bravais lattices.^[16,17] The arrays of circular nanoholes, in comparison to nanobar-based quasicrystal arrays, may offer distinct and additional insights into the aperiodic nature and related magnonics applications because of the following aspects: (1) the isotropic characteristics offered by a circularly shaped basis (via circular holes) as opposed to the two-fold symmetry of the nanobars; (2) interaction among nanobars greatly diminishes for separation greater

S. Watanabe, Dr. V. S. Bhat, K. Baumgaertl, Prof. D. Grundler
École polytechnique fédérale de Lausanne
School of Engineering
Institute of Materials
Laboratory of Nanoscale Magnetic Materials and Magnonics
Lausanne 1015, Switzerland
E-mail: dirk.grundler@epfl.ch

Prof. D. Grundler
École polytechnique fédérale de Lausanne
School of Engineering
Institute of Microengineering
Lausanne 1015, Switzerland

 The ORCID identification number(s) for the author(s) of this article can be found under <https://doi.org/10.1002/adfm.202001388>.

© 2020 The Authors. Published by WILEY-VCH Verlag GmbH & Co. KGaA, Weinheim. This is an open access article under the terms of the Creative Commons Attribution License, which permits use, distribution and reproduction in any medium, provided the original work is properly cited.

DOI: 10.1002/adfm.202001388

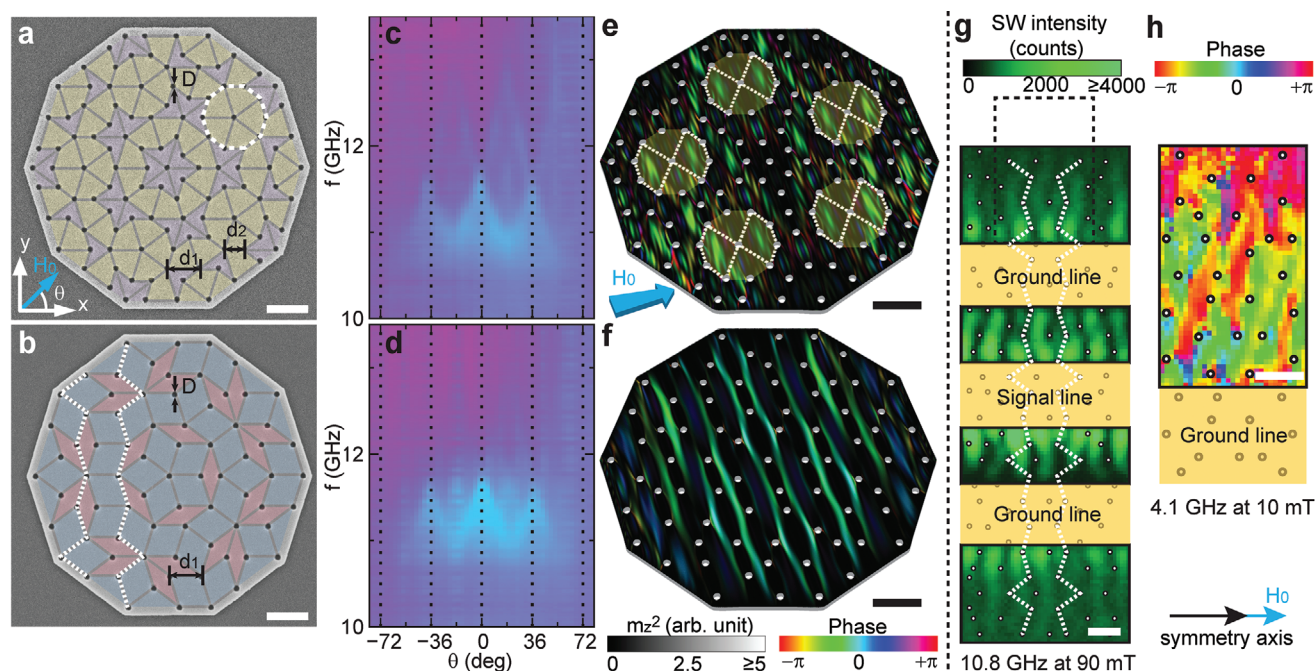


Figure 1. Scanning electron microscopy images of circular nanoholes (dark) patterned on a) Penrose P2 and b) Penrose P3 quasicrystal lattices. The white dotted line in (a) highlights a geometrical motif. The nanoholes are located at the vertices of (a) kites (yellow) and darts (purple), and (b) thick (blue) and thin (pink) rhombi. Colormaps showing experimental angular dependent SW spectra taken on 5th generation (with $D \approx 135$ nm) of c) Penrose P2 and d) Penrose P3 AMQs at $\mu_0 H_0 = 90$ mT. The cyan color indicates resonant absorption (SW modes). Simulated local power map of spin-precessional motion overlaid on top of corresponding phase maps for nanoholes with $D = 135$ nm on 3rd generation e) Penrose P2 (at $f = 11.72$ GHz) and f) Penrose P3 AMQ (at $f = 10.74$ GHz). The field of 90 mT was applied under $\theta = 18$ deg. White dashed lines and semitransparent yellow colored decagons illustrate mirror-symmetric SW motifs arising in the Penrose P2 AMQ in (e). The saturation (gray) and hue color scales in the legend indicate the simulated local power (m_z^2) and phase, respectively, for assumed uniform excitation (standing spin waves). g) Spatial distribution of spin precession (power map) excited at $f = 10.8$ GHz and imaged on a 9th generation Penrose P3 AMQ with $D = 163$ nm. The field of 90 mT was applied along a symmetry axis ($\theta = 0$ deg). Green (black) represents large (small) spin-precessional cone angle. h) Spatially resolved SW phase at $f = 4.1$ GHz propagating in $+y$ -direction in the quasicrystal (hue color) when excited inhomogeneously by the microwave antenna. The field of 10 mT was applied along the symmetry axis ($\theta = 0$ deg). Conway worms are indicated by white dotted lines in (b) and (g). Scale bars indicate 1 μ m.

than 100 nm, thereby making any aperiodic interaction driven application challenging to implement. Irregularities in nanobar shape, size, and placement greatly influence the underlying physical phenomena under investigation. The nanoholes offer enhanced domain wall pinning,^[22] thereby causing an increased switching field, resulting in an increased stability of a device against magnetic field disturbances. Various shapes of holes have been studied on different periodic lattices, such as square shaped and circular holes on a square lattice.^[23–25] Periodic hole lattices support two prominent types of spin-wave mode patterns: localized (confined) and de-localized modes which can form nanochannels^[25] and artificially tailored magnonic minibands.^[26,27] The localized mode patterns occur in the directions perpendicular to the magnetic field and are mostly concentrated at edges of holes (edge modes) or between any two given holes (confined modes). The de-localized modes are connected throughout the ferromagnetic matrix between holes and are perpendicular to the magnetic field direction. These mode patterns appear in a periodic arrangement throughout the lattice. Spin-wave nanochannels exhibit periodically modulated widths. Antidot lattices consisting of periodically arranged holes have hence been investigated thoroughly. Experimental studies on hole arrays with a quasicrystalline arrangement are however missing. Relaxing the condition of periodicity allows one to directly probe the effect of aperiodicity on such type of

patterns and explore their possible application (as reported in this article) due to increased spatial and rotational degrees of freedom. In contrast to photonics and plasmonics,^[10–12] experimental studies on artificial ferromagnetic quasicrystals (AMQs)^[28] which offer unconventional rotational symmetries and a great density of reciprocal vectors are in their infancy.^[21,29,30] Corresponding dynamic magnetic responses in 2D quasicrystals have neither been classified nor fully exploited in view of manipulation and control of magnons.

In this paper, we report combined broadband SW spectroscopy, spatially resolved inelastic (Brillouin) light scattering (BLS) and micromagnetic simulations performed on 2D AMQs (Figure 1a,b). They were prepared from ferromagnetic $\text{Co}_{20}\text{Fe}_{60}\text{B}_{20}$ (CoFeB) thin films by etching out circular nanoholes on the vertices of Penrose P2 and P3 quasicrystal-line tilings^[31,32] (Figure S1–S3, Supporting Information). The CoFeB material was amorphous and magnetically isotropic. We prepared lattices of different generations (Experimental Section), that is, lateral extensions, and with mainly two different nanohole diameters D (Table 1). The arrangement of holes followed characteristic geometrical motifs that exhibited a long range order with ten-fold rotational symmetry. In Figure 1a one motif consists of a decagon (highlighted by a white dotted line) for which a central hole is surrounded by ten holes. The variation of the angle θ of an applied in-plane

Table 1. The CoFeB films were 19 nm thick. The overall area of AMQs increases with the generation. Up to 5th generation, the CPW's signal line width was adjusted to fully cover the AMQs. Errorbars of diameter D of nanoholes indicate the 95% confidence interval of the diameters of ten nanoholes which were randomly chosen from the respective microscopy image.

Sample name	Lattice	Generation	Area [μm^2]	Diameter D [nm]	Number of nanoholes
P2_SH_3rdGen	P2	3rd	7.0×7.4	134 ± 6	121
P2_LH_3rdGen	P2	3rd	7.0×7.4	227 ± 5	121
P2_SH_4thGen	P2	4th	11.0×11.6	137 ± 7	301
P2_LH_4thGen	P2	4th	11.0×11.6	216 ± 3	301
P2_SH_5thGen	P2	5th	17.5×18.5	144 ± 15	761
P2_LH_5thGen	P2	5th	17.5×18.5	215 ± 13	761
P2_SH_9thGen ^{a)}	P2	9th	117.5×123.6	159 ± 6	34 101
P2_LH_9thGen ^{a)}	P2	9th	117.5×123.6	242 ± 6	34 101
P3_SH_3rdGen	P3	3rd	7.0×7.4	134 ± 6	76
P3_LH_3rdGen	P3	3rd	7.0×7.4	219 ± 5	76
P3_SH_4thGen	P3	4th	11.0×11.6	133 ± 11	191
P3_LH_4thGen	P3	4th	11.0×11.6	218 ± 7	191
P3_SH_5thGen	P3	5th	17.5×18.5	137 ± 9	476
P3_LH_5thGen	P3	5th	17.5×18.5	221 ± 12	476
P3_SH_9thGen ^{a)}	P3	9th	117.5×123.6	163 ± 5	21 106
P3_LH_9thGen ^{a)}	P3	9th	117.5×123.6	234 ± 4	21 106

^{a)}The CPW signal line width was two microns and smaller than the lateral extension of the AMQ in case of 9th generation.

magnetic field H_0 induced SW branches of resonant microwave absorption that exhibited ten-fold angular symmetry (Figure 1c,d). This symmetry is not known from periodic lattices with translational invariance and substantiates the quasicrystalline nature of the nanohole lattices. At fixed θ we observe multiple SW branches in experiments and simulations. We identify spin precession in fundamental motifs (Figure 1e) that do not depend on the generation and are distinctly different from the geometrical ones forming the tilings. Moreover, the aperiodic nanoholes give rise to stripe-like excitations in simulations (Figure 1f) and experiments (Figure 1g). These magnon nanochannels incorporate aperiodic sequences of bends. This aperiodicity is not known from previously investigated periodic hole lattices and might generate magnon band structures that vary from channel to channel, contrary to periodic counterparts.^[25] The discovered aperiodic sequences of bends are similar to the Conway worms (white dotted lines in Figure 1b,g) which represent an established mathematical concept when modeling quasicrystals. These worms form aperiodic Fibonacci chains in the 2D Penrose tilings.^[6–8] By BLS we obtain direct images of propagating magnons (Figure 1h) that exhibit irregular wavefronts across neighboring nanochannels which change with magnon frequency. These real-space images taken on a 2D analogue of a natural quasicrystal^[32] thereby provide fundamental insight into the formation of wave-like states in quasicrystalline matter. The discovered magnon modes fuel a new class of metamaterials by which irregular worm-like channels transform into a real-world application such as a dense wavelength division multiplexer (DWDM). Going beyond photonics, the magnonic DWDM is ultra-compact, reconfigurable via a rotating field and driven by an electromagnetic wave at a single input frequency.

2. Result and Discussion

2.1. Standing Spin Waves in Artificial Ferromagnetic Quasicrystal

SW spectroscopy was performed by a vector network analyzer connected to a coplanar waveguide (CPW) integrated on top of ten nominally identical AMQs of a given generation (Figure S2, Supporting Information). Penrose P2 and P3 AMQs (Figure 1a,b, and Table 1) both have ten-fold rotational symmetry but exhibit distinct differences concerning the prototiles used to construct them. In a P2 tiling (Figure 1a) the seed tiles are a kite and a dart. In a P3 tiling (Figure 1b) one considers thick and thin rhombi,^[6] forming a 2D analogue of a natural icosahedral quasicrystal.^[32] Two inter-vertex distances are present in a P2 tiling (we used $d_1 = 810$ nm and $d_2 = 500$ nm) as opposed to only one inter-vertex distance in Penrose P3 tiling (we used $d_1 = 810$ nm). The P2 tiling incorporates a lattice point (nanohole) density that is larger by 62% compared to P3. For the nanofabrication we kept the inter-vertex distances constant (see above) and thereby created AMQs covering larger and larger areas from generation to generation (Table 1). Figure 1a,b (Figure 1c,d) refer to AMQs P2_SH_3rdGen and P3_SH_3rdGen (P2_SH_5thGen and P3_SH_5thGen), respectively, with nanoholes (H) of small (S) diameter $D \approx 135$ nm located at the vertices of 3rd (5th) generation (AMQs of 5th generation P2 and P3 tilings are shown in Figure S1, Supporting Information). The angle-dependent SW spectra in Figure 1c,d evidence magnetic anisotropy^[33] and a ten-fold rotational symmetry. This rotational symmetry is expected for an infinitely large Penrose lattice. The pronounced variation of resonance frequencies f with θ reflects the variation of the effective magnetic field H_{eff} which enters the equation of motion of spin precession.^[33] We note that according to the Curie

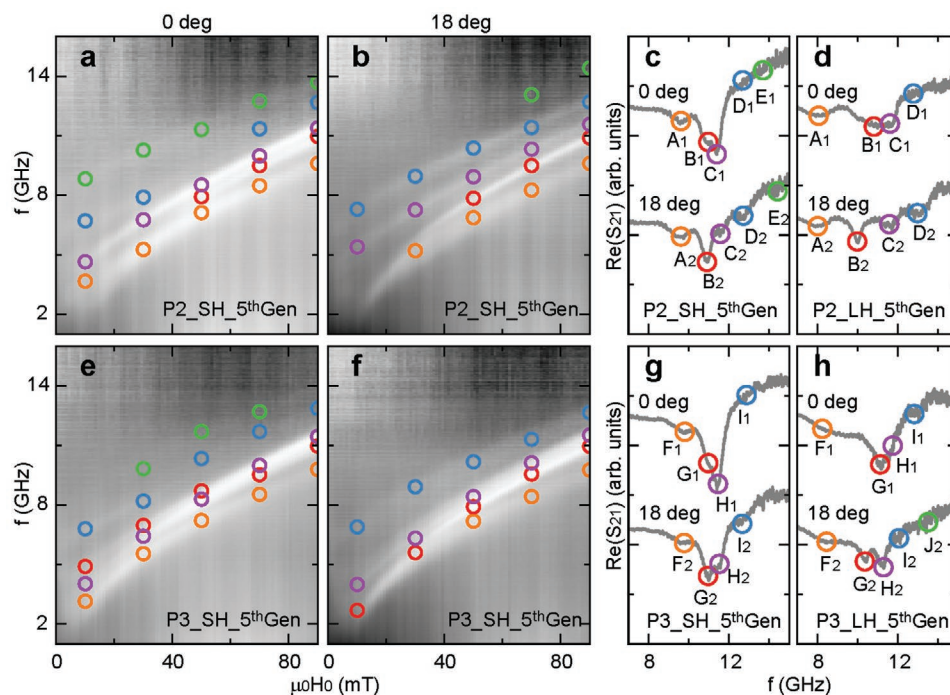


Figure 2. Field dependent spectroscopy on 5th generation Penrose AMQs. Grayscale-coded spectra for samples P2_SH_5thGen at a) $\theta = 0$ deg, and b) $\theta = 18$ deg; line spectra at 90 mT for c) P2_SH_5thGen, and d) P2_LH_5thGen at two angles; spectra for P3_SH_5thGen at e) $\theta = 0$ deg, and f) $\theta = 18$ deg; line spectra at 90 mT for g) P3_SH_5thGen, and h) P3_LH_5thGen at two different angles. Colored symbols in the experimental spectra in (c), (d), (g), (h) indicate the frequency values which are consistent with the different branches identified in the grayscale plots (a), (b), (e), (f).

principle,^[34] we expect a ten-fold rotational symmetry of SW resonances also for small-area five-fold rotationally symmetric AMQs due to the linear polarization of the radio-frequency field in the CPW. This field is composed of, both, left- and right-circularly polarized electromagnetic waves. The two components allow us to excite gyrotropic spin precession for opposing directions of a magnetic field^[33] and opposing spin-precessional motion in one and the same segment of the AMQ. Hence, SW resonances in a five-fold rotationally symmetric geometrical motif exhibit a ten-fold rotational symmetry with respect to θ .^[19]

Figure 2a,b shows field-dependent SW spectra for the 5th generation AMQ P2_SH_5thGen at $\theta = 0$ and 18 deg, respectively. Five prominent SW branches A_1 , B_1 , C_1 , D_1 , and E_1 for $\theta = 0$ deg and A_2 , B_2 , C_2 , D_2 , and E_2 for $\theta = 18$ deg are observed whose frequencies increase with H_0 (Figure 2c). We note that similar branches were detected when exploring AMQs of 3rd and 4th generation (Figures S4 and S5, Supporting Information). These branches exist independent of the total lateral size. Comparison of Figure 2a,b reveals that the SW resonances are “separated” more clearly from each other when the field was applied along $\theta = 18$ deg, that is, along an off-symmetry axis of the AMQ. Spectra taken on AMQ P3_SH_5thGen (Figure 2e,g) for $\theta = 0$ deg reveal four prominent branches F_1 , G_1 , H_1 , and I_1 . The resonances F_2 , G_2 , H_2 , and I_2 at small D (Figure 2f,g) are again partly better resolved for $\theta = 18$ deg compared to $\theta = 0$ deg. We note that resonances in the P3 AMQ (Figure 2f) were less well resolved compared to the P2 AMQ (Figure 2b). This was surprising as the Penrose P3 AMQ contained 62% less nanoholes that would act as scattering centers compared to P2 AMQ.

For AMQs with a large (L) hole diameter spectra are shown in Figure 2d,h (and in Figure S5, Supporting Information). Clearer spectra also occurred for large hole diameters in P2 AMQs at 18 deg (Figure 2d). Some resonances are systematically shifted in frequency and are less pronounced in P2_LH (P3_LH) compared to P2_SH (P3_SH) AMQs. We attribute these observations to the larger nanohole diameter (i) modifying H_{eff} via the demagnetization effect and (ii) reducing the area covered by ferromagnetic material, respectively.

2.2. Emergent Magnonic Motifs and Worm-Like Nanochannels Explored by Micromagnetic Simulation

To get a microscopic understanding of the experimental observations, we performed micromagnetic simulations. The simulated power spectrum for AMQ P2_SH_3rdGen at $\theta = 0$ deg suggests five distinct modes (Figure 3a). The number and frequencies agree well with SW resonance frequencies obtained experimentally (Figure S6, Supporting Information). Due to the inhomogeneous magnetic field created by the demagnetization effect (Figure S7, Supporting Information), several spin-wave modes of different eigenfrequencies are excited: Local phase and power maps indicate that branch A_1 reflects edge modes (not shown) with spin precession close to the edges of nanoholes. Branch B_1 (Figure 3b) contains stripe-like extended modes which remind one of modes seen in periodic nanohole lattices. However, in case of a P2 AMQ with a high density of vertices the stripe-like modes are multi-segmented as nanoholes selectively block spin precession at some places. Branch

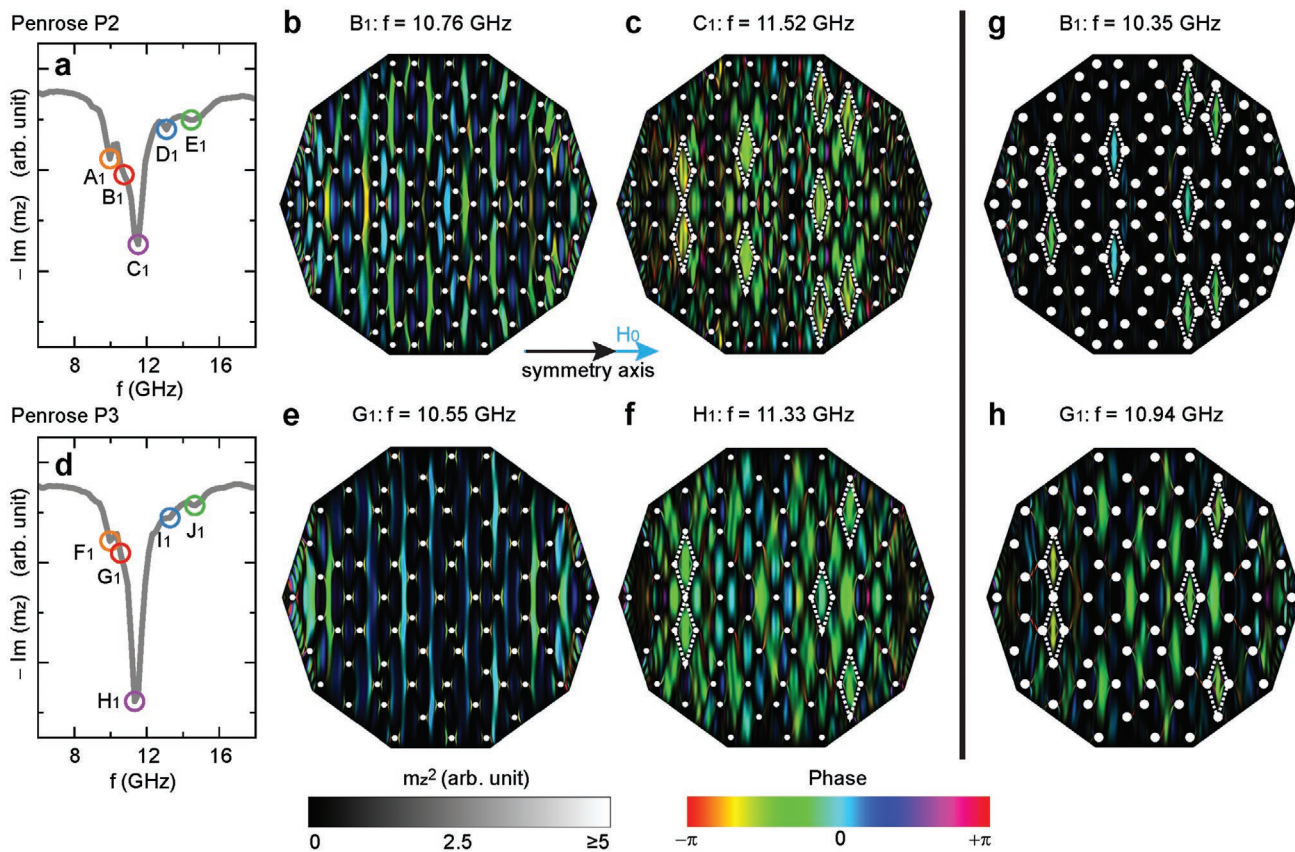


Figure 3. Micromagnetic simulations for an applied field of 90 mT along $\theta = 0$ deg (symmetry axis) of P2 and P3 AMQs and comparison of nanohole diameters. a) Simulated SW spectrum ($\text{Im}(m_z)$) of Penrose P2 AMQ with nanoholes of small diameter $D = 135$ nm. Circles and labels are chosen corresponding to resonance frequencies seen in experiments. Power (m_z^2) map overlaid on corresponding local phase maps indicating origins of modes b) B_1 (Penrose P2 AMQ), and c) C_1 (P2 AMQ). d) Spectrum of AMQ P3_SH_3rdGen, and maps of spin-precessional motion of modes e) G_1 (P3 AMQ), and f) H_1 (P3 AMQ). Dashed lines highlight spin precession surrounded by four nanoholes (rhombi). Gray and hue color scales represent the power and phase, respectively. In (b) and (e) an enhanced contrast is used to identify stripe-like SW excitations (nanochannels). Magnonic mode motifs found in (g) P2 and (h) P3 AMQ with large diameter ($D = 220$ nm).

C_1 (Figure 3c) contains patches of pronounced excitations that appear to be confined between, for example, four holes (indicated by rhombi with dotted white lines). Note that the overall mode pattern exhibits a strict mirror symmetry with respect to the horizontal central axis of the AMQ, which is parallel to the applied field. Branches D_1 and E_1 are attributed to higher order confined modes (not shown). In the case of a P3_SH_3rdGen AMQ, we extract five salient modes (Figure 3d). Based on the simulations we classify them as follows: F_1 (edge mode), G_1 (extended modes shown in Figure 3e), H_1 (patches of confined modes shown in Figure 3f), I_1 and J_1 (higher order confined modes, not shown). Differences between P2_SH and P3_SH AMQs for a field along $\theta = 0$ deg are as follows: (1) stripe-like modes in P2 are blocked in many locations, whereas in P3 nanochannels extend more through the structure. (2) Patches highlighted with white dotted lines in Figure 3c,f represent a mode motif of magnons confined in thin rhombi. Importantly, AMQs with enlarged nanohole diameters repeat this rhombus-like mode motif confined between only four holes: For both P2 in Figure 3g and P3 in Figure 3h they are clearly visible; the additional holes in P2 compared to P3 suppress spin-precessional motion in large parts and reduce the magnon mode pattern

to the rhombus-like motif almost completely (Figure 3g). We emphasize that the rhombus is a geometrical motif for P3, but not for P2. The observation of an identical magnon motif in P2 and P3 AMQs hints towards the emergence of magnon mode motifs different from the underlying geometrical motifs. (3) Simulated resonances in P2 (Figure 3a) are slightly better resolved as compared to P3 (Figure 3d) consistent with experiments.

For AMQ P2_SH_3rdGen (Figure 4a) and AMQ P3_SH_3rdGen (Figure 4e) with H_0 applied at $\theta = 18$ deg we identify five modes in the corresponding simulations. The resonance frequencies are in good agreement with the experimentally observed branches at 90 mT (Figure S6, Supporting information). The signal strengths of SW resonances B_2 to D_2 are comparable to one another in contrast to signals obtained for $\theta = 0$ deg on P2 (Figure 3a). In the experiments corresponding branches at $\theta = 18$ deg were indeed better resolved compared to $\theta = 0$ deg. Branch B_2 (Figure 4b) reflects stripe-like modes extending in a direction transverse to the applied field direction. In Figure 4b–d we indicate the decagon-like geometrical motif enclosed by ten nanoholes which is highlighted by a white dotted line in Figure 1a. Thereby a one-to-one

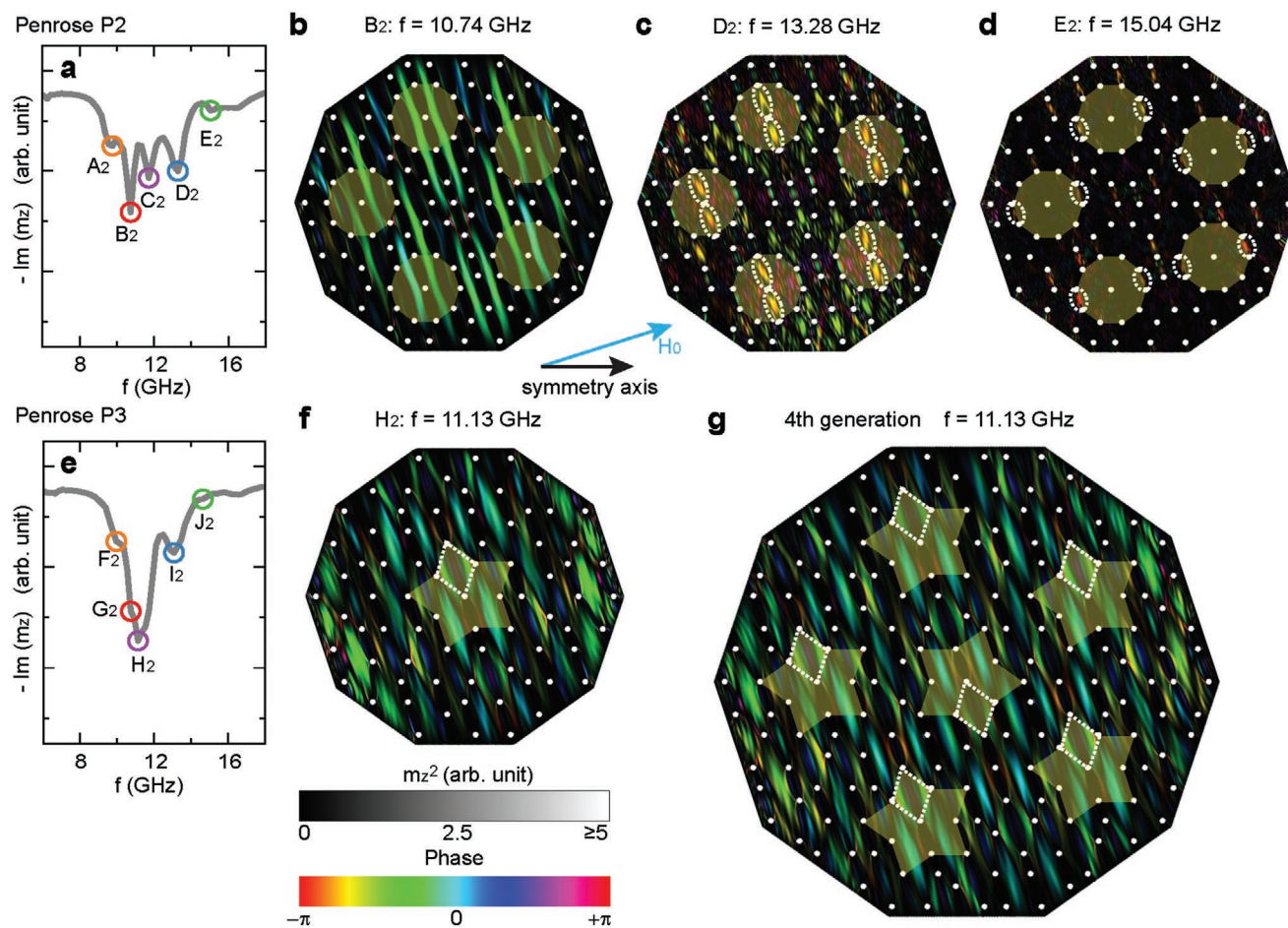


Figure 4. Micromagnetic simulations for an applied field of 90 mT along $\theta = 18$ deg (off-symmetry axis) of P2 and P3 AMQs and comparison of nanohole diameters. a) Simulated SW spectrum ($\text{Im}(m_2)$) of Penrose P2_SH_3rdGen with nanoholes of diameter $D = 135$ nm. Circles and letters are consistent with labels introduced for experimental data. Power maps (m_2^2) overlaid on corresponding local phase maps indicating regions of spin-precessional motion in P2 for branches b) B₂, c) D₂, d) E₂. e) Spectrum simulated for an AMQ P3_SH_3rdGen and spin-precessional motion of f) H₂ at $f = 11.13$ GHz in a 3rd generation AMQ. g) Spin-precessional motion at the same frequency in P3_SH_4thGen, that is, a 4th generation AMQ. A mirror symmetry becomes apparent for the localized mode patches (highlighted white dotted lines). The yellow semi-transparent decagons and stars revisit underlying geometrical motifs for P2 and P3, respectively.

comparison between geometrical (structural) and mode motifs can be performed. In Figure 4b, close to the center of the geometrical motifs the modes exhibit bends. The bends imply that the aperiodically arranged nanoholes make propagation in SW nanochannels highly sensitive to the nanohole diameter (Figure S8, Supporting Information). For P2 AMQs, we find the SW nanochannels to be multi-segmented. This is different for P3 AMQs: In Figure 1f (and P3_LH in Figure S8 in the Supporting Information), long 1D nanochannels are identified that exhibit bends separated by different distances. Their appearances resemble worms whose bends vary from channel to channel. The aperiodicity prohibits identical sequences of holes within neighboring nanochannels suggesting channel-dependent magnon states. The minimum width of a nanochannel analyzed along a Conway worm (highlighted by white dots in Figure 1b) amounts to 50 nm. Due to this confinement spin waves in the nanochannels are in the exchange-dominated regime,^[33] and therefore the anisotropy of spin waves induced by the dipolar interaction in the long wavelength limit is not

responsible for the existence of the worm-like nanochannels. We expect narrower nanochannels for further decreased inter-vertex distances in the Penrose tiling as the spin-wave dispersion relation is isotropic in the exchange regime.^[33] Furthermore, dissecting a Conway worm (Experimental Section) creates another Conway worm.^[6] Interestingly there is always at least one Conway worm in the Penrose tiling produced by the matching rule,^[6] which can propagate through the entire lattice. In case of low-damping material such nanochannels are expected to transmit spin-wave signals from edge to edge. Our experiment shows that inside the bulk of the AMQ there are many more aperiodic nanochannels guiding spin waves than these very long edge-connecting worms. We attribute our observation to the infinite set of worms of short and long ties that are expected for a regular Penrose tiling.^[6] The worms are distributed according to the Fibonacci sequence.

Higher frequency excitations in P2 AMQ at $\theta = 18$ deg resemble narrow patches of pronounced spin-precessional motion as indicated by the white dotted lines in the simulation

results: The patches appear within (Figure 1e and Figure 4c) or at the edges of the geometrical motifs (Figure 4d). The well-defined patches can be understood in analogy to periodic antidot lattices^[25,29] in which standing magnon modes reflected confinement and localization due to edges of nanoholes and inhomogeneities of H_{eff} ,^[35] respectively. We note that the emergent magnonic mode motifs seen in Figures 1e and 4b–d all exhibit a mirror symmetry axis being perpendicular to the applied field. A consistent mirror symmetry axis is found for mode patches of P3 at $\theta = 18$ deg (Figures 1f and 4f,g). Axes of mirror symmetries thus depend on the orientation of H_0 consistent with a report about nanobar-based quasicrystals.^[19] Figure 4f,g substantiates that a SW motif identified in generation three of AMQ P3 (dashed white rhombus) occurs in generation four at structurally similar positions within the geometrical motif (highlighted by the yellow star). Emergent magnon motifs identified throughout this work thus reflect self-similar motifs reappearing in different generations of quasicrystals.

2.3. Wavelength Division Multiplexing Utilizing Worm-Like Nanochannels

Using BLS microscopy (Figure S3, Supporting Information) we evidenced spin-precessional motion in the aperiodically bent nanochannels (Figure 1g). Data were taken near a CPW by which we excited the magnons. In the experiment, we observed a minimum width of 300 nm which is larger than the predicted value of 50 nm. The discrepancy is attributed to the diffraction limit of micro-focus BLS as explained in ref. [36]. Regions of large spin-precessional motion varied as a function of frequency and field orientation as will be discussed in the following (see also Figures S9 and S10, Supporting Information). Large segments of worm-like nanochannels were resolved best at relatively low frequency consistent with simulations. BLS with phase resolution allows us to directly image the phase evolution of waves in the quasicrystalline structure when excited by the integrated microstructured CPW. We evidence irregular wavefronts of propagating SWs (Figures 1h and 5a–c) indicating that magnon states are different from nanochannel to nanochannel. The wavefronts vary significantly with excitation frequency. The lengths over which the phase $k(x, y) \cdot \gamma$ varies by 2π in nanochannels vary with frequency (vertical bars in Figure 5a–c). $k(x, y)$ is the wave vector of spin waves which is not constant along a nanochannel as it depends on the aperiodically modulated effective field $H_{\text{eff}}(x, y)$.^[33] The irregular phase evolution (wavefront) is in contrast to 2D periodic antidot lattice magnonic crystals^[25] for which spin waves in neighboring nanochannels are in phase and wavefronts are parallel to the CPW if the applied magnetic field direction is collinear with the CPW's signal line. The SW band structures for each nanochannel are identical due to the translational invariance of the magnonic crystals. In AMQs each SW nanochannel is modulated by a different sequence of nanoholes thanks to the quasicrystalline nature. Note that the arrangement of nanoholes is related to a 1D Fibonacci sequence, which suggests the formation of a specific spin-wave band structure.^[37] For the same spin-precessional frequency differently propagating magnon states are thereby

created on a single chip in neighboring nanochannels. They enable dense wavelength division multiplexing (Figure S11, Supporting Information). In photonics, a DWDM allows one to exploit numerous wavelengths of light on a single optical fiber. For photons wavelength and frequency are coupled via the speed of light and hence a corresponding number of different input frequencies is required. In the quasicrystal-based DWDM only a single input frequency is needed to generate different wavelengths. Going beyond photonics the configuration of the magnonic DWDM can be altered ("gated") by an applied magnetic field. Another gating device such as a phase shifter using local magnetic fields^[38] could be used to tune wavefronts of spin waves in the quasicrystal, and in turn, the phase differences between neighboring nanochannels (Figure S11, Supporting Information) would be modified. This would create a wave-based logic device with a large number of both processing units and outputs which offers an areal density much larger than the recently proposed (de)multiplexers.^[39,40] Thanks to the scale invariance of demagnetization fields, further down-scaling of the size of the magnonic DWDM is possible. In Figure 5d we demonstrate the rotation of the extended modes in nanochannels experimentally by choosing $\theta = 90$ deg for BLS performed at an excitation frequency of 11.2 GHz. The observed rotation of channels goes beyond the photonic channels (waveguides) created by tailored defects in hyperuniform disordered solids which are fixed in space.^[41] The extended magnon modes transform into localized excitations in the experiment when we increase the frequency to 12.9 GHz (Figure 5e). The transformation is predicted by simulations. Localized modes were found in theoretical studies also in bi-component magnonic AMQs.^[28]

3. Conclusion

In our study, spin waves in 2D AMQs are thoroughly investigated using broadband all-electrical spectroscopy, spatially resolved inelastic light scattering and micromagnetic simulations. Scale invariant spin-wave spectra indicate the emergence of peculiar magnon mode patterns in 2D AMQs which we characterize by the simulations. They exhibit specific mirror symmetries different from the underlying quasicrystalline lattices. The mirror symmetry axis varies with the direction of the applied field H_0 and takes either zero or 90 deg with respect to H_0 . The unconventional rotational symmetries of AMQs is reflected in the angular dependent SW spectra. In analogy to their plasmonic counterparts,^[10] the aperiodically arranged nanoholes could be exploited in grating couplers, that is, microwave-to-magnon transducers. Their unconventional rotational symmetries are advantageous in order to optimize multi-directional magnon emission relevant for integrated magnonic circuits.^[17,18] Particularly intriguing are the aperiodically bent nanochannels which we observed. For them we find a width down to 50 nm in simulations. Due to the quasiperiodic arrangement of the nanoholes, spin-wave states are expected to be different from nanochannel to nanochannel. Consistently we detect irregular wavefronts of spin waves in the AMQs using spatially resolved BLS. They are created due to an inhomogeneous internal field H_{eff} which is not active in

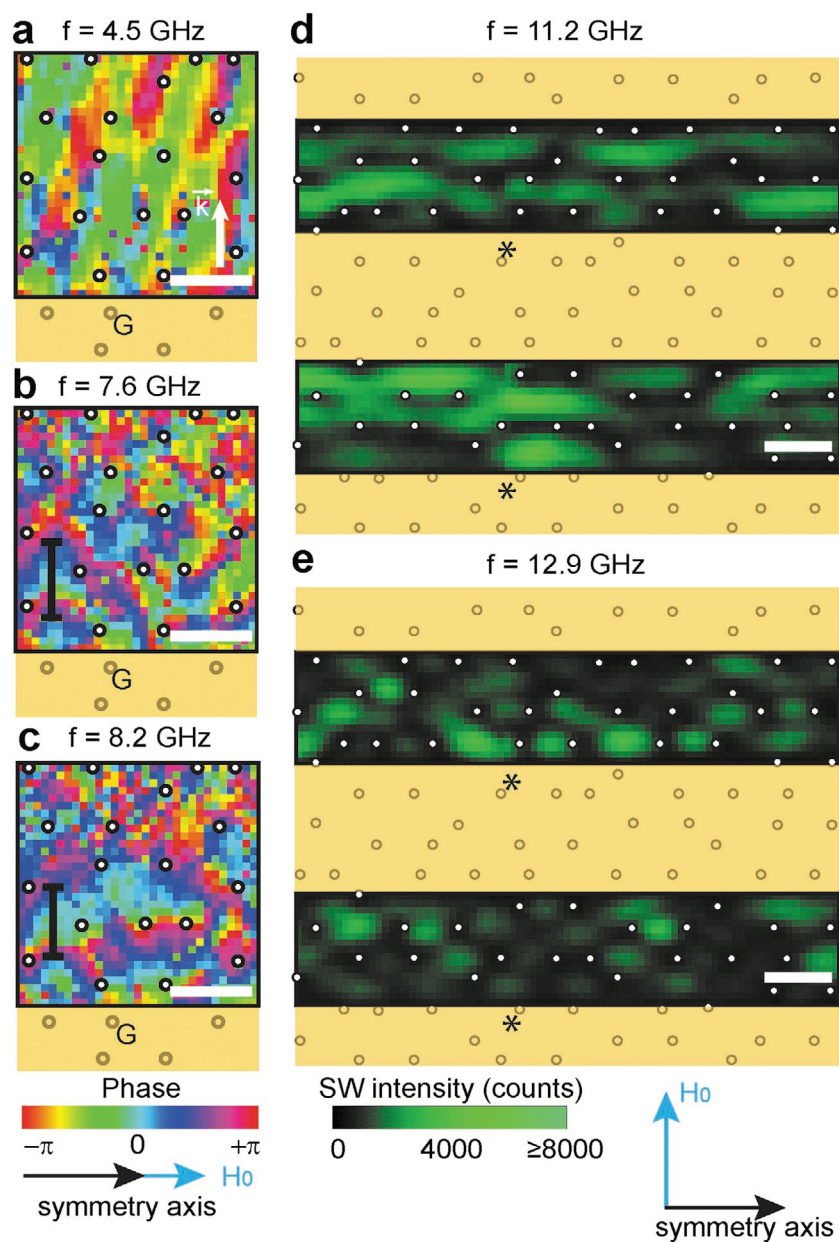


Figure 5. Phase-resolved magnon propagation in a quasicrystal and control of nanochannels. Spatially resolved phase evolution of spin waves propagating along k (white arrow in (a)) in the P3 quasicrystal of Figure 1h at a) 4.5 GHz, b) 7.6 GHz, and c) 8.2 GHz for 10 mT. The black vertical bars indicate a phase difference of 2π . The length of the bar can be attributed to the wavelength in the selected channel. d) Worm-like nanochannels (bright) imaged by BLS without phase resolution at an excitation frequency of 11.2 GHz for $\theta = 90$ deg and 90 mT. This angle is consistent with the channel configuration shown in Figure 1f. e) BLS imaging at an increased frequency of 12.9 GHz. The spin-precessional motion is found to be confined to narrow patches. The scale bars are $1 \mu\text{m}$. The asterisk marks a position where there was a slight stitching error in the x, y positioning system.

photonics and plasmonics. The materials-by-design approach and imaging by a state-of-the-art microscopy technique allowed us to explore the implication of Conway worms defined for the theoretical description of quasicrystals concerning a real-world application. We propose a quasicrystal-based DWDM that can be operated at a single microwave frequency and is ultra-compact because of the significant wavelength reduction inherent to magnonics.

4. Experimental Section

Creation of Penrose P2 and P3 AMQs: Figure S12a, Supporting Information shows the methodology behind constructing Penrose P2 tilings of different generation (and overall size). The authors started with two prototiles, called kites and darts. A kite is a quadrilateral with four interior angles of $72^\circ, 72^\circ, 72^\circ,$ and 144° ; a dart is a quadrilateral with four internal angles of $36^\circ, 72^\circ, 36^\circ,$ and 216° . In this study, the authors began with the configuration formed by joining five kites at

a common vertex; this configuration called “0th generation”. Next, each kite was dissected into two smaller kites and a dart, and rejoined according to the matching rule^[6] to obtain the 1st generation tiling. Each application of such dissection rule generated a tiling of a higher generation containing a correspondingly larger number of prototypical elements. The 1st generation tiling was rescaled to make it the same size as the 0th generation tiling; kites and darts of the 1st generation were smaller in size, compared to those of the 0th generation. Continued dissection and rescaling produced higher-generation Penrose P2 tilings, and the deflation process was then terminated at desired finite generation.

In the case of Penrose P3 tilings (Figure S12b, Supporting Information), it was started with two rhombi that have equal edges but different angles: (1) Thick rhombus with interior angles of 72°, 108°, 72°, and 108°. (2) Thin rhombus with interior angles of 36°, 144°, 36°, and 144°. Here, the authors started with the configuration formed by joining ten acute Robinson triangles (half of thin rhombi) at a common vertex; this configuration we termed “0th generation”. Two neighboring acute Robinson triangles were bisected into one thin and one thick rhombi that leads to “1st generation” P3 tiling. Subsequently, each thick rhombus was dissected into two thick and one thin rhombi; whereas thin rhombus got divided into one thick and thin rhombi, and were attached together according to matching rules,^[6] producing next generation of Penrose P3 tiling. As in the case of P2 tiling, we rescaled the thick and thin rhombi so that the subsequent generation thick and thin rhombi were of smaller sizes as compared to ones in 0th generation.

Finally, the edges of kites and darts were taken out and inserted nanoholes on vertices of kites and darts in P2 tiling. In the case of P3 tiling edges of rhombi were taken out and inserted nanoholes. The next step was to convert the final P2 and P3 tilings into a GDS file format that was imported into commercial electron beam lithography (EBL) software.

Sample Fabrication: A 19 nm thick amorphous CoFeB (Co₂₀Fe₆₀B₂₀) thin film was sputtered^[42] on a Si substrate. The aperiodic nanohole masks were patterned on hydrogen silsesquioxane negative electron beam resists using EBL. Ion beam etching was then performed to form a decagonal mesa and open the nanoholes in the magnetic thin film to form different AMQs as summarized in Table 1. Consecutively, CPW were patterned via EBL, electron beam evaporation of Ti/Au, and lift-off processing. They covered ten nominally identical AMQs parallel to their symmetry axis. The saturation magnetization was determined using SW spectroscopy on a reference CoFeB film, and amounted to 1.8 T. The widths of the signal line of CPW were 9, 13, and 20 μm for AMQs on Penrose tilings of 3rd, 4th, and 5th generation, respectively.

Broadband Spin-Wave Spectroscopy: SW excitations in AMQs were studied via all electrical SW spectroscopy. The two ends of the CPW (patterned on top of the AMQs, Figure S2, Supporting Information) were connected to a vector network analyzer (VNA) to sweep the frequency and record the absorption spectra. The samples resided in a custom built 2D vector magnet assembly that allowed us to vary the in-plane angle θ of the applied field H_0 . A 2-port VNA allowed us to generate a microwave magnetic field with frequencies ranging from 10 MHz to 26.5 GHz. The applied microwave current generated an in-plane rf-magnetic field perpendicular to the long axis of the CPW. The microwave with a power of 0 dBm was applied at the port 1 of the CPW in order to excite magnetization precession. The precession-induced voltage was detected at port 2 via reading the scattering parameter S_{21} where the numbers 2 and 1 in the subscript denote the detection and excitation port. An external magnetic field $\mu_0 H_0$ of up to 90 mT was applied under an angle θ between the external field H_0 and the CPW's long axis. In order to increase signal to noise ratio, $\Delta S_{21} = S_{21}(H_0) - S_{21}(\text{Ref})$ was evaluated where $S_{21}(H_0)$ and $S_{21}(\text{Ref})$ represent scattering parameters measured at a given field H_0 and at 90 mT along $\theta = 90^\circ$, respectively.

Brillouin Light Scattering Microscopy: Spin-wave eigenmodes were imaged via Brillouin light scattering (BLS) microscopy with and without phase resolution at room temperature using a setup similar to refs. [43,44]. Figure S3, Supporting Information shows the experimental

setup. The end of one CPW was electrically bonded to a printed-circuit board, which was connected to a signal generator applying a microwave current. The corresponding magnetic microwave field excited spin precession in the AMQ close to the CPW at a fixed frequency. The power was such that spin precession was excited in the linear regime. A magnetic field of 90 mT was applied under an angle θ via a permanent magnet for BLS measurement without phase resolution. For phase-resolved BLS measurement, a magnetic field of 10 mT was applied after that a field of 90 mT was applied in order to first saturate the AMQ. A lens with a numerical aperture of 0.85 was used to focus a 473 nm wavelength with a spot size of 300 nm onto the AMQ. Laser power was set to 1 and 0.85 mW for BLS measurement without and with phase resolution, respectively. Energy shifts of reflected laser light due to the inelastic magnon-photon scattering were detected by a triple-tandem Fabry–Prot interferometer. The AMQ was positioned under the laser with a spot using x, y piezo-positioning system. The step size to acquire the images of Figures 1g,h and 4, Figures S9 and S10, Supporting Information was 100 nm. We exploited phase-resolved inelastic light scattering while exciting spin waves phase-coherently at the straight CPW. As the CPW was microstructured the excitation was inhomogeneous and generated propagating spin waves with a finite wave vector k . The acquisition time of inelastically scattered photons outside the CPW was chosen to be 2.14 times longer than in regions between signal and ground lines to compensate for the different excitation strength near a CPW. The 120 nm thick Au layer of the CPW did not allow us to monitor a signal from the magnonic channels underneath the ground and signal lines. The nanohole positions depicted in Figure 1g were reconstructed in that we overlaid (i) atomic force microscopy (AFM) images taken on the studied AMQ with (ii) the optical image taken in the BLS microscope, (iii) the BLS data, and (iv) the exposure masks for CPWs and electron beam lithography of nanoholes. Characteristic notches and dust particles identified in AFM and BLS microscopy data were used for a pre-alignment of the nanohole lattices. Finally we adjusted precisely the lattice of nanoholes given by the exposure mask relative to BLS data. Still we shifted this mask only within about 200 nm in lateral directions (i.e., by less than the diameter of the laser spot) to avoid that a maximum BLS intensity peak resided inside a hole with a diameter of about 200 nm.

Simulations: Micromagnetic simulations using OOMMF^[45] were performed to obtain a microscopic insight into SW excitations in AMQs. A bitmap containing the required P2 and P3 geometry was imported into OOMMF and discretized on a grid of 10 nm × 10 nm × 19 nm. A global in-plane 90 mT DC magnetic field was applied along the x direction, and equilibrium magnetization configuration was determined. Subsequently, a spatially homogeneous Gaussian pulse of 20 mT amplitude and 2.5 ps duration was applied along the z -axis (out of plane). In the simulation we explored the standing spin-wave modes due to uniform excitation. The perpendicular component of magnetization m_z was recorded as a function of x, y and the time step. A fast Fourier transformation (FFT) was performed on the magnetization of each pixel along the time axis to obtain the resonance spectrum. Then sums of power and phase of m_z were calculated to display the SW spatial profile for relevant frequencies. $\text{Im}(m_z)$ was then integrated over the whole geometry, and plotted as a function of frequency f in order to observe the microwave absorption. $\text{Im}(m_z)$ corresponds to the S_{21} observed in experiment. The input parameters used in the simulations were as follows: saturation magnetization $\mu_0 M_S = 1.8$ T, exchange constant $A = 13 \times 10^{-12}$ J m⁻¹, and damping constant 0.007. In simulations, the global magnetic field was fixed along x -axis and the relevant bitmap containing the geometry was oriented at 0° and 18°. To illustrate the spatial distribution of spin-precessional motion under uniform excitation we show maps of the local phase and power (square of the spin precessional amplitude m_z). The widths of nanochannels in simulations (experiments) were extracted in that we followed the amplitudes of spin-precessional motion along a Conway worm with a step size of 10 nm (100 nm). At each step we extracted the full width at half maximum of the local amplitude distribution in the corresponding spin-wave nanochannel.

Supporting Information

Supporting Information is available from the Wiley Online Library or from the author.

Acknowledgements

The research was supported by the SNSF via grant number 163016.

Conflict of Interest

The authors declare no conflict of interest.

Keywords

magnonics, metamaterials, nanomagnets, quasicrystals, spin waves

Received: February 13, 2020

Revised: June 2, 2020

Published online:

-
- [1] D. Shechtman, Nobel Lecture, Stockholm December, **2011**.
- [2] D. P. DiVincenzo, P. J. Steinhardt, in *Quasicrystals: The State of the Art, Series on Directions in Condensed Matter Physics*, vol. 16, World Scientific Publishing Company, Farrer Road, Singapore **1999**.
- [3] M. Bayindir, E. Cubukcu, I. Bulu, E. Ozbay, *Europhys. Lett.* **2001**, 56, 41.
- [4] D. P. DiVincenzo, in *Physical Models of Perfect Quasicrystal Growth*, vol. 229, Plenum Press, New York **1990**.
- [5] M. Ronchetti, M. Bertagnolli, M. V. Jaric, in *Generation and Dynamics of Defects in Two-Dimensional Quasicrystals*, vol. 229, Plenum Press, New York **1990**.
- [6] M. Gardner, *Penrose Tiles to Trapdoor Ciphers: And the Return of Dr. Matrix*, The Mathematical Association of America, Washinton, DC **1997**.
- [7] H. Au-Yang, J. H. H. Perk, *Indagat. Math.* **2013**, 24, 996.
- [8] F. Fang, D. Hammock, K. Irwin, *Crystals* **2017**, 7, 304.
- [9] P. J. Steinhardt, P. M. Chaikin, W. Man, (Princeton University) *US 8064127B2*, **2011**.
- [10] T. Matsui, A. Agrawal, A. Nahata, Z. V. Vardeny, *Nature* **2007**, 446, 517.
- [11] J.-M. Dubois, *Isr. J. Chem.* **2011**, 51, 1168.
- [12] Z. V. Vardeny, A. Nahata, A. Agrawal, *Nat. Photonics* **2013**, 7, 177.
- [13] A. Chumak, A. Serga, B. Hillebrands, *J. Phys. D: Appl. Phys.* **2017**, 50, 244001.
- [14] V. V. Kruglyak, S. O. Demokritov, D. Grundler, *J. Phys. D: Appl. Phys.* **2010**, 43, 264001.
- [15] S. A. Nikitov, Ph. Tailhades, C. S. Tsai, *J. Magn. Magn. Mater.* **2001**, 236, 320.
- [16] A. Chumak, A. Serga, B. Hillebrands, *Nat. Commun.* **2014**, 5, 4700.
- [17] H. Yu, G. Duerr, R. Huber, M. Bahr, T. Schwarze, F. Brandl, D. Grundler, *Nat. Commun.* **2013**, 4, 2702.
- [18] H. Yu, O. d'Allivy Kelly, V. Cros, R. Bernard, P. Bortolotti, A. Anane, F. Brandl, F. Heimbach, D. Grundler, *Nat. Commun.* **2016**, 7, 11255.
- [19] V. S. Bhat, D. Grundler, *Phys. Rev. B* **2018**, 98, 174408.
- [20] D. Shi, Z. Budrikis, A. Stein, S. A. Morley, P. D. Olmsted, G. Burnell, C. H. Marrows, *Nat. Phys.* **2018**, 14, 309.
- [21] V. S. Bhat, J. Sklenar, B. Farmer, J. Woods, J. T. Hastings, S. J. Lee, J. B. Ketterson, L. E. De Long, *Phys. Rev. Lett.* **2013**, 111, 077201.
- [22] X. Zhou, G. L. Chua, N. Singh, A. O. Adeyeye, *Adv. Funct. Mater.* **2016**, 26, 1437.
- [23] M. J. Pechan, C. Yu, R. L. Compton, J. P. Park, P. A. Crowell, *J. Appl. Phys.* **2005**, 97, 10J903.
- [24] J. Sklenar, V. S. Bhat, L. E. DeLong, O. Heinonen, J. B. Ketterson, *Appl. Phys. Lett.* **2013**, 102, 152412.
- [25] S. Neusser, B. Botters, D. Grundler, *Phys. Rev. B* **2008**, 78, 054406.
- [26] S. Neusser, G. Duerr, S. Tacchi, M. Madami, M. L. Sokolovsky, G. Gubbiotti, M. Krawczyk, D. Grundler, *Phys. Rev. B* **2011**, 84, 094454.
- [27] R. Zivieri, S. Tacchi, F. Montoncello, L. Giovannini, F. Nizzoli, M. Madami, G. Gubbiotti, G. Carlotti, S. Neusser, G. Duerr, D. Grundler, *Phys. Rev. B* **2012**, 85, 012403.
- [28] J. Rychły, S. Mieszczak, J. Kos, *J. Magn. Magn. Mater.* **2018**, 450, 18.
- [29] S. Choudhury, S. Barman, Y. Otani, A. Barman, *ACS Nano* **2017**, 11, 8814.
- [30] F. Lisiecki, J. Rychły, P. Kuświk, H. Głowiński, J. W. Kłos, F. Groß, N. Träger, I. Bykova, M. Weigand, M. Zelent, E. J. Goering, G. Schütz, M. Krawczyk, F. Stobiecki, J. Dubowik, J. Gräfe, *Phys. Rev. Appl.* **2019**, 11, 054061.
- [31] R. Penrose, *Math. Intell.* **1979**, 2, 32.
- [32] L. Bursill, P. J. Lin, *Nature* **1985**, 316, 50.
- [33] A. Gurevich, G. Melkov, *Magnetization Oscillations and Waves*, CRC Press, Boca Raton, FL **1996**.
- [34] K. Brading, E. Castellani, *Symmetries in Physics: Philosophical Reflections*, Cambridge University Press, Cambridge, UK **2003**.
- [35] J. Jorzick, S. O. Demokritov, B. Hillebrands, M. Bailleul, C. Fermon, K. Y. Guslienko, A. N. Slavin, D. V. Berkov, N. L. Gorn, *Phys. Rev. Lett.* **2002**, 88, 047204.
- [36] K. Wagner, A. Kákay, K. Schultheiss, A. Henschke, T. Sebastian, H. Schultheiss, *Nat. Nanotechnol.* **2016**, 11, 432.
- [37] F. Lisiecki, J. Rychły, P. Kuświk, H. Głowiński, J. W. Kłos, F. Groß, I. Bykova, M. Weigand, M. Zelent, E. J. Goering, G. Schütz, G. Gubbiotti, M. Krawczyk, F. Stobiecki, J. Dubowik, J. Gräfe, *Phys. Rev. Appl.* **2019**, 11, 054003.
- [38] K. S. Lee, S. K. Kim, *J. Appl. Phys.* **2008**, 104, 053909.
- [39] K. Vogt, F. Y. Fradin, J. E. Pearson, T. Sebastian, S. D. Bader, B. Hillebrands, A. Hoffmann, H. Schultheiss, *Nat. Commun.* **2014**, 5, 3727.
- [40] F. Heussner, G. Talmelli, M. Geilen, B. Heinz, T. Brächer, T. Meyer, F. Ciubotaru, C. Adelman, K. Yamamoto, A. A. Serga, B. Hillebrands, P. Pirro, *Phys. Status solidi-R* **2020**, 14, 1900695.
- [41] M. Florescu, P. J. Steinhardt, S. Torquato, *Phys. Rev. B* **2013**, 87, 165116.
- [42] D. Ruffer, M. Slot, R. Huber, T. Schwarze, F. Heimbach, G. Tütüncüoğlu, F. Matteini, E. Russo-Averchi, A. Kovács, R. Dunin-Borkowski, R. R. Zamani, J. R. Morante, J. Arbiol, A. Fontcuberta i Morral, D. Grundler, *APL Mater.* **2014**, 2, 076112.
- [43] V. E. Demidov, S. O. Demokritov, *IEEE Trans. Magn.* **2015**, 51, 1.
- [44] T. Sebastian, K. Schultheiss, B. Obry, B. Hillebrands, H. Schultheiss, *Front. Phys.* **2015**, 3, 35.
- [45] M. J. Donahue, D. G. Porter, *OOMMF User Guide, Version 1.0*, National Institute of Standards and Technology, Gaithersburg, MD **1999**.